Fusion Engineering and Design 159 (2020) 111957

Contents lists available at ScienceDirect

Fusion Engineering and Design

journal homepage: www.elsevier.com/locate/fusengdes

Control pathway for an advanced divertor on ITER

J.T. Wai [a], P.J. Vail [a], E. Kolemen [a,b,*]

[a] Princeton University, Princeton, NJ 08544, USA
[b] Princeton Plasma Physics Laboratory, Princeton, NJ 08543, USA

ARTICLE INFO

Keywords:
X-divertor
Flux expansion
Shape control
Model predictive control

ABSTRACT

This paper presents the development of a coupled shape and divertor controller for ITER with capabilities to control the flux expansion and an advanced divertor configuration, the x-divertor (XD), in which a secondary x-point is placed in the downstream scrape-off layer. Due to the high-performance nature of ITER and its relatively few shaping coils, satisfying constraints on the coil currents, power supplies, and plasma shape is a challenge for this configuration. To meet these constraints the controller uses the constrained linear quadratic regulator (CLQR) framework [1], a variant of model predictive control (MPC). Previous work [2] has shown the existence of XD equilibria on ITER and in this study, we identify a control pathway for achieving the "pure" XD where the secondary x-point is placed at the outer strike point, representing a maximally flux-expanding scenario. Constraints are observed throughout the transition. One limitation is that at high flux expansion, the shallow angle of incidence of the magnetic field on the divertor results in a reduced plasma wetted area via tile shadowing. On the other hand, the high flux expansion and flaring characteristic of the XD facilitate enhanced detachment, which could negate the shadowing effect to some degree. In this case it would be desirable to operate as close to the flux expansion limit as possible. To this end we also demonstrate the controller's ability to track a trajectory for the flux expansion near the accepted angle of incidence limit.

1. Introduction

Managing power exhaust at the plasma-material interface is a critical challenge for next-gen tokamaks such as ITER and DEMO, with much effort focused on keeping heat flux below the solid material limit of 10 MW/m^2. One strategy is to make use of so-called advanced divertor geometries such as the snowflake divertor (SFD) [3], x-divertor (XD) [4], and super x-divertor (SXD) [5]. Briefly, these strategies decrease heat flux by increasing the poloidal flux expansion and plasma wetted area, among other mechanisms.

The in-place strategy for ITER does not use an advanced divertor and instead relies on the standard x-point divertor, vertical targets, and operation in the partially detached regime [6]. However, while not considered in the original design, more recent work [2] has shown the existence of some x-divertor equilibria on ITER. This opens up the possibility of experimenting with XD scenarios on ITER in the event that the in-place heat flux strategy has unforeseen issues, or more likely, as a test case for future reactors. There is some historical precedent for this in that NSTX [7], DIII-D [8], and EAST [9] have made major originally-unplanned-for upgrades to the divertor in order to explore alternative and higher power scenarios. The upgrade on EAST, for example, was motivated by the desire to operate with higher scrape-off layer (SOL) power and considers a Nearby-Double-Null (similar to the XD) configuration. If it were possible to test an advanced divertor scenario on ITER, this could provide valuable information for e.g., DEMO, which has called for investigation into advanced divertors and liquid metal divertors [10] (an interesting possibility is combining both concepts, since liquid metals can tolerate extremely low strike point angles which is a concern of the XD).

In this work we explore the possibility of the XD configuration on ITER from a control perspective. Other advanced divertors are not suitable candidates for ITER since the SXD would require geometric changes to the machine, and the SFD requires excessive coil currents [11]. The XD is defined by the presence of a secondary x-point in the SOL near the target plate. This forms a region of low poloidal field near the target, increasing the SOL connection length and connection length gradient (flaring). The XD can modestly increase plasma-wetted area (limited by a shadowing effect of the tiles) but the main advantages as compared to the standard divertor relate to detachment. The XD detaches at lower density and features improved detachment front stability

* Corresponding author.
E-mail addresses: jwai@princeton.edu (J.T. Wai), ekolemen@princeton.edu (E. Kolemen).

https://doi.org/10.1016/j.fusengdes.2020.111957
Received 21 May 2020; Received in revised form 19 July 2020; Accepted 13 August 2020
Available online 6 September 2020

[2,4,12]. Since divertor density has a negative effect on core confinement, in the XD, core performance can remain roughly constant for deeper levels of detachment. As mentioned, others have shown that equilibria exist but this does not necessarily guarantee a large subspace of XD equilibria or a robust control pathway for the XD. The control pathway must take into consideration the plasma dynamics and limits on the superconducting coil system and power supplies. In this study we develop a model predictive controller and apply this to the shape and divertor control problem on ITER. We investigate several aspects of advanced divertor control including flux expansion control, secondary x-point formation, and transition during rampup.

The isoflux method [13] is used to perform both the shape and divertor control. For shape control, target boundary points for the shape are specified (see Fig. 3), and the coil currents are adjusted so that the flux at these points is equal to the flux at the boundary. By divertor control we mean controlling various aspects of the divertor configuration such as the flux expansion, x-point positions, and strike point locations. Since these quantities are defined by the flux distribution, the underlying model for shape and divertor control is equivalent.

Traditionally, advanced divertor controllers such as those used on NSTXU and DIII-D [14–18] have used decoupled schemes for shape and divertor control. That is, while the control algorithms are certainly able to mix shape and divertor control coils, in practice this is not done since the machines have an abundance of actuators. These controllers also used proportional-integral-derivative (PID) and linear-quadratic-regulation (LQR) methods. Because of the relatively fewer control actuators on ITER (11 independent poloidal field coil circuits), and the large distances from coils to plasma, the shape and divertor control scheme for ITER must be coupled. Additionally, actuator limits become more constricting as the machine size increases. Initial testing found that the control pathway and actuator limits were too difficult to navigate with LQR methods, motivating the use of model predictive control (MPC) for this study. Specifically, we use a variant of MPC known as constrained LQR (CLQR) [1], so called because the controller gains are identical to LQR if the constraints are inactive.

As discussed in [19,2] the high flux expansion characteristic of the XD cannot by itself solve the heat flux problem. In general, to protect tile edges from receiving parallel heat flux, there is a lower limit on the incident angle that total magnetic field makes with the divertor target, generally accepted as $\geq 1^\circ$ for an attached plasma. On ITER, the divertor monoblocks are oriented so as to not expose edges, although at low strike point angles this leads to a reduced plasma wetted area via shadowing. These considerations limit the applicability of XD scenarios.

However, a well-known benefit of high flux expansion is enhanced detachment. That is, for a given upstream density, radiative power at the target is increased. If higher levels of detachment can be obtained with the XD, the shadowing effect would be reduced since a larger fraction of the heat is transferred via volumetric processes (illustrated in Fig. 2 of [2]). An additional benefit of the XD is related to poloidal flaring, as quantified by the divertor index DI_{SOL} defined in [4], which measures the increase in flux expansion moving from x-point to strike point. This has been theorized to increase the detachment window and improve detachment front stability [20,4,12]. Experiments on DIII-D showed that the XD led to detachment onset at 10–20% lower upstream density which was attributed partially to high DI_{SOL}, since this preferentially adds SOL connection length near the target. Thus, while tile shadowing is a strong concern it may be possible to increase flux expansion, flaring, and detachment synergistically and reduce the strike point angle limit.

The rest of this paper is organized as follows. Sections 2 and 3 describe the shape control model and its use in the MPC framework. In Section 5.1 we use the controller to simulate flux expansion control when operating near the 1° strike point angle limit. In Section 5.2 we explore the extreme case that this limit can be ignored and identify a control pathway for a maximally flux-expanding configuration. This simulation includes x-point formation, rampup, and movement of the secondary x-point up to the divertor plate to create the pure XD. We find that this pure XD configuration can be obtained for a 10 MA plasma while satisfying constraints on the coil currents, voltages, and other parameters listed in Table 1 throughout the transition. Section 6 concludes.

2. Review of the shape control model

Without a coil set for Ohmic current, the shape control system on ITER has three tasks: controlling the plasma current, controlling shape, and stabilizing the plasma vertical position. Vertical stabilization (VS) control is necessary due to the plasma vertical instability, which occurs on the resistive wall time scale (200ms), whereas current and shape control (CSC) take place on the timescale of multiple seconds. Due to the timescale separation, the control objectives can be designed independently (Fig. 2) with CSC taking place in the outer loop and VS taking place in the inner loop. Many successful control strategies have been designed in this way [21–27].

2.1. Dynamics model

Our interest is in developing a state-space dynamics model for the CSC loop so that MPC can be readily applied. Each circuit loop in the system—including the PF control coils, vacuum vessel elements, and the plasma itself—is taken to follow the standard circuit equation

$$v_s = R_s I_s + M_{ss}\dot{I}_s + \dot{\Psi}_{ss,plasma} \tag{1}$$

With $s \in \{c, v, p\}$ representing the coils, vessel elements, and plasma. R represents the internal resistance of the circuit loop and M is the mutual inductance between the loop and all other circuit loops. The complicating term is $\dot{\Psi}_{ss,plasma}$ which represents the flux change in the loop due to spatial movement and redistribution of the plasma current. This is in general a non-linear function where the plasma redistribution must satisfy the Grad–Shafranov equation. We now linearize this term around a nominal equilibrium, and introduce the notation

$$X_{ab} := \left.\frac{\partial \Psi_{a,plasma}}{\partial I_b}\right|_{eq(t)} \tag{2}$$

so that

$$\dot{\Psi}_{ab,plasma} = \left.\frac{\partial \Psi_{a,plasma}}{\partial I_b}\right|_{eq(t)} \delta\dot{I}_b = X_{ab}\delta\dot{I}_b \tag{3}$$

Table 1
Inequality constraints used in the pathway scenario (Section 5.2), with the activated constraints highlighted. $\dot{P}$ and P are the total power derivative and power applied to the coils. The activated control point gaps 10, 16 and 17 correspond to gaps on the upper-inboard and upper-outboard regions.

Activated Constraints				
PF Coils			Outputs	
Coil #	I	V	--	
PF1	< 48 kA	< 1.5 kV	$\dot{P}$	< 200 MW/s
PF2	< 55 kA	< 1.5 kV	P	< 250 MW
PF3	< 55 kA	< 1.5 kV	r_{strike}	on plate
PF4	< 55 kA	< 1.5 kV	z_{strike}	on plate
PF5	< 52 kA	< 1.5 kV	cp_{1-9}	gaps > 10 cm
PF6	< 52 kA	< 1.5 kV	cp_{10}	gap > 10 cm
CS1U	< 45 kA	< 1.5 kV	cp_{11-15}	gaps > 10 cm
CS1L	< 45 kA	< 3.0 kV	cp_{16}	gap > 10 cm
CS2U			cp_{17}	gap > 10 cm
CS2L	< 45 kA	< 1.5 kV	cp_{18-31}	gaps > 10 cm
CS3U	< 45 kA	< 1.5 kV		
CS3L	< 45 kA	< 1.5 kV		

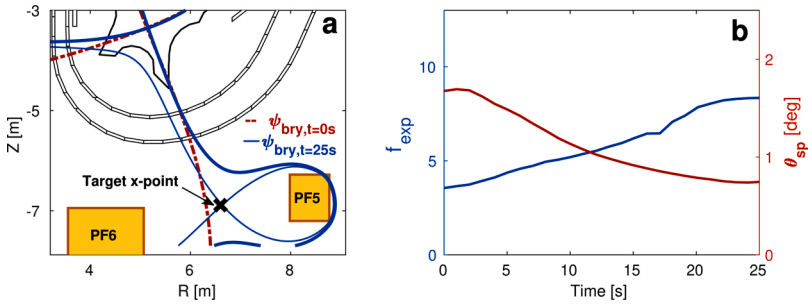

Fig. 1. (a) Transition from the standard divertor (SD) to the x-divertor (XD) in the pathway scenario (Section 5.2) with plasma current $I_p = 4$ MA. In the SD there is a strong gradient in the flux between coils PF5 and PF6. To create the XD, a secondary x-point is formed by controlling the flux gradient to zero at a target location between these coils. (b) Evolution of the flux expansion and $I_p = 15$MA equivalent strike point angle ($\sin(\theta_{sp}) \propto B_p \propto I_p$) during the transition. If limited to 1° one would stop the evolution at an intermediate time.

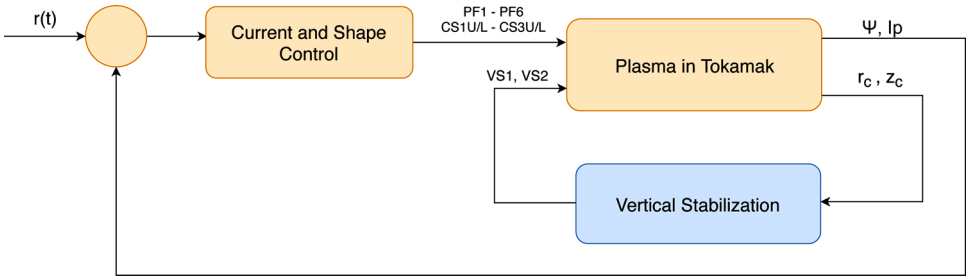

Fig. 2. Current, shape, and position control diagram for ITER. Shaping occurs over multiple seconds while the inner loop (VS) controls the ≈200 ms vertical instability.

The values of the flux response matrix X_{ab} are obtained using the non-rigid linear plasma response model **gspert** [28] integrated in the General Atomics based TokSys environment [29]. In this model, changes in the shape of the plasma and in the distribution of current are accounted for by explicitly perturbing the Grad–Shafranov equation at a particular equilibrium. By writing Eq. (1) for all circuits in the system, in the linearized frame we obtain

$$\begin{bmatrix} \delta v_c \\ 0 \\ 0 \end{bmatrix} = \begin{bmatrix} R_c & & \\ & R_v & \\ & & R_p \end{bmatrix} \begin{bmatrix} \delta I_c \\ \delta I_v \\ \delta I_p \end{bmatrix} + \begin{bmatrix} M_{cc} & M_{cv} & M_{cp} \\ M_{vc} & M_{vv} & M_{vp} \\ M_{pc} & M_{pv} & M_{pp} \end{bmatrix} \begin{bmatrix} \delta \dot{I}_c \\ \delta \dot{I}_v \\ \delta \dot{I}_p \end{bmatrix} + \begin{bmatrix} X_{cc} & X_{cv} & X_{cp} \\ X_{vc} & X_{vv} & X_{vp} \\ X_{pc} & X_{pv} & X_{pp} \end{bmatrix} \begin{bmatrix} \delta \dot{I}_c \\ \delta \dot{I}_v \\ \delta \dot{I}_p \end{bmatrix} \tag{4}$$

This is easily rewritten in standard state space form

$$\begin{aligned} \delta \dot{I} &= A(t)\delta I + B(t)\delta v \\ A(t) &= -(M + X(t))^{-1} R \\ B(t) &= (M + X(t))^{-1} \end{aligned} \tag{5}$$

For this work, we focus primarily on developing the outer current and shape control loop. For the inner VS loop, we follow the method detailed further in Section 4 of [21]. The voltage applied to the VS coils is found by feeding back on the plasma velocity and VS coil currents

$$\delta v_{vs} = \begin{bmatrix} k_D & k_I \end{bmatrix} \begin{bmatrix} \dot{z}_p \\ \delta I_{vs} \end{bmatrix} := k_{vs} \begin{bmatrix} \dot{z}_p \\ \delta I_{vs} \end{bmatrix} \tag{6}$$

where $\dot{z}_p$ is the velocity of the vertical position of the plasma current centroid, δI_{vs} is the current in the VS coils, and $k_{vs} = [k_D\ k_I]$ are the controller gains (see [21]). The feedback outputs are estimated from the output response model

$$\begin{bmatrix} \dot{z}_p \\ \delta I_{vs} \end{bmatrix} = C_{vs}(t)\delta I \tag{7}$$

So that the dynamics model (Eq. (5)) can be rewritten as

$$\begin{aligned} \delta \dot{I} &= A(t)\delta I + b_{vs}(t)\delta v_{vs} + B_{pf}(t)\delta v_{pf} \\ &= [A(t) + b_{vs}(t)k_{vs}C_{vs}(t)]\delta I + B_{pf}(t)\delta v_{pf} \\ &:= A_{stabilized}(t)\delta I + B_{pf}(t)\delta v_{pf} \end{aligned} \tag{8}$$

The $B(t)$ matrix has been divided into components corresponding to the control voltages of the vertical stabilization (subscript vs) coils and the shaping poloidal field (subscript pf) coils. Eq. (8) represents the current dynamics as seen by the outer loop. We use this as the model for developing the shape controller, while for simulations we use the full model with the vertical stabilization feedback.

2.2. Output model

In this section we derive an output model of the form $y = C\delta I$ in order to perform effective current and shape control and perform reference tracking of the secondary x-point. For shape control, we use the isoflux method and define 31 control segments and control points which determine the target shape (Fig. 3). The poloidal flux is measured at each control point with the goal of regulating it to be equal to the flux at the plasma boundary. We define an error vector between the measured and desired outputs as

$$\begin{aligned} e(t) &= Z(t) - Z_D(t) \\ Z(t) &= [\delta I_c \quad I_p \quad r_x \quad z_x \quad r_{strike} \quad z_{strike} \quad \psi_{cp\times 31}]^T \\ Z_D(t) &= [0 \quad I_{pD} \quad r_{xD} \quad z_{xD} \quad r_{strikeD} \quad z_{strikeD} \quad \psi_{bry\times 31}]^T \end{aligned} \tag{9}$$

where δI_c is the vector of perturbed coil currents (included so that current changes are penalized), I_p is the plasma current, (r_x, z_x, r_{strike}, z_{strike}) are the vectors for x-point and strike point locations, $\psi_{cp\times 31}$ is the vector of flux levels associated with the 31 control points, and ψ_{bry} is the flux quantity defining the plasma boundary. The subscript D denotes a desired value for that quantity. Perturbing e at a nominal equilibrium gives the output equation with $y = \delta e$

$$\delta e = \begin{bmatrix} \frac{\partial (Z - Z_D)}{\partial I_c} & \frac{\partial (Z - Z_D)}{\partial I_v} & \frac{\partial (Z - Z_D)}{\partial I_p} \end{bmatrix} \begin{bmatrix} \delta I_c \\ \delta I_v \\ \delta I_p \end{bmatrix} \Leftrightarrow y = C(t)\delta I \tag{10}$$

The above derivatives are obtained using the non-rigid plasma response model [28]. More detail on these calculations is given in Section 2.3. Note that, with the exception of $\psi_{bry\times 31}$, all the elements of Z_D have partial derivatives equal to 0, since most of the targets are preset and not dependent on the states. The control objective is to drive the error vector to 0. Using

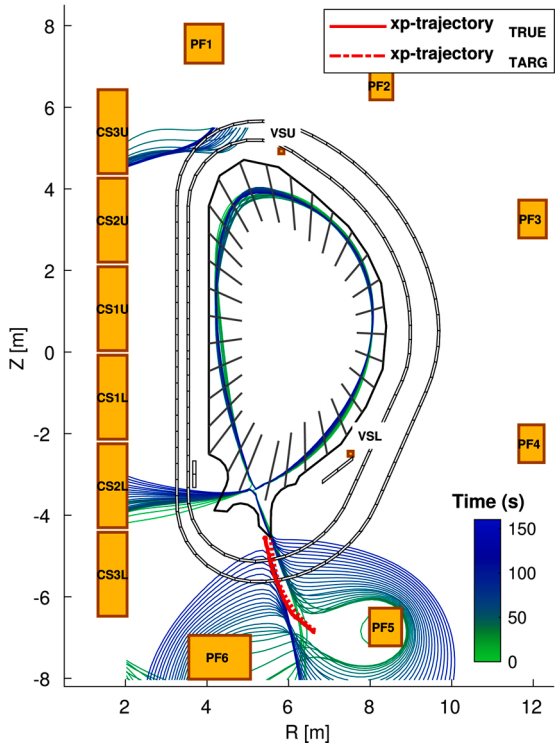

Fig. 3. Evolution of the plasma boundary in the pathway scenario (Section 5.2) showing movement of the secondary x-point into the "pure" x-divertor configuration. The controller maintains plasma shape to a high degree while accommodating large changes to the magnetic geometry in the divertor region. Lines intersecting the plasma boundary correspond to the shape control segments.

$$e = e_0 + \delta e \tag{11}$$

We see that this is a reference-tracking problem for y with reference trajectory

$$r = -e0 \tag{12}$$

The control objective is now set up as a standard state-space reference-tracking problem as defined by Eqs. (8), (10), (12).

2.3. X-point derivatives

In this section we obtain expressions for the spatial movement of the x-points, $\frac{\partial r_x}{\partial I_s}$ and $\frac{\partial z_x}{\partial I_s}$ which is important for good tracking behavior. This method performs a simple derivative expansion and a cubic convolution of the grid point flux and flux response.

At the x-point the flux gradient is zero $\nabla\psi(\vec{x}) = 0$. If the flux is perturbed slightly, Newton's method would find the new x-point by solving

$$\nabla\psi(\vec{x}) = 0 \approx J_F(\vec{x_0})(\vec{x} - \vec{x_0}) + \nabla\psi(\vec{x_0}) \tag{13}$$

where $J_F(\vec{x_0})$ is the Jacobian of $\nabla\psi(\vec{x_0})$. Taking the derivative of Eq. (13) with respect to the coil currents can be written

$$\begin{aligned} \frac{\partial \vec{x}}{\partial I} &= -J_F^{-1}(\vec{x_0})\frac{\partial \nabla\psi(\vec{x_0})}{\partial I} \\ &= -J_F^{-1}(\vec{x_0})\begin{bmatrix} \partial_r\partial_I\psi(\vec{x_0}) \\ \partial_z\partial_I\psi(\vec{x_0}) \end{bmatrix} \end{aligned} \tag{14}$$

The derivatives on the RHS $\partial_I\psi$ were computed at the grid points via the nonrigid response model, and we can perform a cubic convolution to obtain the value at the desired location. Following the method of Keys [30] the convolution is applied first in the radial direction and then in the vertical direction. When the grid points around the x-point are indexed from −1 to 2 this gives

$$b_i = \frac{1}{2}\begin{bmatrix} 1 & d_r & d_r^2 & d_r^3 \end{bmatrix}\begin{bmatrix} 0 & 2 & 0 & 0 \\ -1 & 0 & 1 & 0 \\ 2 & -5 & 4 & -1 \\ -1 & 3 & -3 & 1 \end{bmatrix}\begin{bmatrix} \partial_I\psi(-1,i) \\ \partial_I\psi(0,i) \\ \partial_I\psi(1,i) \\ \partial_I\psi(2,i) \end{bmatrix}$$

$$\partial_I\psi(r,z) = \frac{1}{2}\begin{bmatrix} 1 & d_z & d_z^2 & d_z^3 \end{bmatrix}\begin{bmatrix} 0 & 2 & 0 & 0 \\ -1 & 0 & 1 & 0 \\ 2 & -5 & 4 & -1 \\ -1 & 3 & -3 & 1 \end{bmatrix}\begin{bmatrix} b_{-1} \\ b_0 \\ b_1 \\ b_2 \end{bmatrix} \tag{15}$$

The variables d_r and d_z are simply the radial and vertical positions of the x-point normalized to the grid cell spacing:

$$\begin{aligned} d_r &= r \bmod \Delta r \\ d_z &= z \bmod \Delta z \end{aligned} \tag{16}$$

3. Model predictive control

In MPC, beginning with an initial state, the state-space equations are used to predict the system behavior a finite number of steps into the future. Then, a mathematical optimization problem is solved over the prediction window, minimizing a cost function of the predicted outputs and inputs and accounting for inequality constraints. This process is often computationally intensive but has been shown to be sufficiently rapid for shape control [31]. First, the shape control dynamics (Eq. (8)) are converted to discrete time using the zero-order hold method. For presentation clarity, we drop the subscripts of Eq. (8) and relabel the state and control vectors $\delta I = x$ and $\delta v = u$. The discrete time dynamics are then

$$\begin{aligned} x_{k+1} &= A_k x_k + B_k u_k \\ y_k &= C_k x_k \end{aligned} \tag{17}$$

3.1. Cost function and prediction model

The cost function at the current time step is taken to be

$$J_k = \sum_{i=1}^{N}\left[(y_{k+i} - r_{k+i})^T Q_i (y_{k+i} - r_{k+i}) + u_{k+i-1}^T R_i u_{k+i-1}\right] \tag{18}$$

N is the look ahead number for the prediction model and is set to correspond to a prediction window of 9–10 s. We found that larger prediction windows increased computation without improving performance, since the model is time-varying and far-future predictions are not as accurate, while smaller prediction windows did not adequately plan around the constraints. For example, aggressive path-following with a prediction window of 4 s in the flux expansion scenario (Section 5.1) led the plasma to a dead-end state where the boundary gaps could not be met within coil current limits. Q_i and R_i are weighting matrices for the output errors and actuator usage at each time step, and are held constant except for the case of Q_N. That is, $R_i = R$ and $Q_{i,i\neq N} = Q$. Since we use the Constrained Linear Quadratic Regulation (CLQR) algorithm, Q_N is obtained as the solution to the discrete time algebraic Riccati equation which can be solved with the MATLAB **dare** function.

$$Q_N = Q + A^T Q_N A - (A^T Q_N B)(R + B^T Q_N B)^{-1}(B^T Q_N A) \tag{19}$$

The cost function can be expressed more efficiently as

$$J_k = \hat{Y}^T \hat{Q} \hat{Y} - 2\hat{r}^T \hat{Q} \hat{Y} + \hat{U}^T \hat{R} \hat{U} \tag{20}$$

$$\begin{aligned} \hat{Y} &= \left[y_{k+1}^T \ldots y_{k+N}^T\right]^T, \quad \hat{r} = \left[r_{k+1}^T \ldots r_{k+N}^T\right]^T, \quad \hat{U} = \left[u_k^T \ldots u_{k+N-1}^T\right]^T, \\ \hat{Q} &= \text{blockdiag}\left(Q_1 \ldots Q_N\right), \quad \hat{R} = \text{blockdiag}\left(R_1 \ldots R_N\right) \end{aligned}$$

We now find a prediction model for $\widehat{Y}$, with the intention of writing the cost function in terms of the control inputs only. Using the model Eq. (17) we find

$$\begin{bmatrix} y_{k+1} \\ y_{k+2} \\ \vdots \\ y_{k+N} \end{bmatrix} = \underbrace{\begin{bmatrix} \mathrm{C\ A} \\ CA^2 \\ \vdots \\ CA^N \end{bmatrix}}_{E} x_k + \underbrace{\begin{bmatrix} \mathrm{C\ B} & & & \\ \mathrm{C\ AB} & \mathrm{C\ B} & & \\ \vdots & \vdots & \ddots & \\ CA^{N-1}B & CA^{N-2}B & \dots & \mathrm{CB} \end{bmatrix}}_{F} \begin{bmatrix} u_k \\ u_{k+1} \\ \vdots \\ u_{k+N-1} \end{bmatrix}$$

Or equivalently

$$\widehat{Y} = \mathrm{E}x_k + F\widehat{U} \tag{21}$$

Upon substituting the prediction model Eq. (21) into Eq. (20), and using the symmetry properties of $\widehat{Q}$ and $\widehat{R}$, the cost function optimization is written in the standard form of a convex quadratic program (QP):

$$\underset{\widehat{U}}{\text{minimize}} \quad J_k = \widehat{U}^T H \widehat{U} + 2f^T \widehat{U} + J_\theta \tag{22}$$

$$H = F^T \widehat{Q} F + \widehat{R}, \quad f = F^T \widehat{Q}\left(\mathrm{E}x_k - \widehat{r}\right)$$

J_θ is a collection of terms that are invariant to feedback and can be set to 0 without changing the optimization. Once coupled with the constraints, the optimization is solved using **mpcqpsolver** in MATLAB though many other commercial and free solvers exist that can perform this optimization.

3.2. Constraints

The ITER tokamak has a number of constraints that must be satisfied by the current and shape controller (Table 1). Most importantly, to prevent damage to the machine the PF coil currents must stay below their nominal limits. Since the PF current deviations are included in the output vector, this is a type of output constraint. Output constraints are also used to prevent the plasma from straying too close to the wall. In terms of the isoflux method, this is equivalent to specifying a maximum flux error that the plasma can have at any control point. We must now manipulate the physical constraints so that they are functions of the optimization variables. In particular, since the control model was written in the linearized system, we must transform the constraints to the linearized system.

*Input constraints:*Input voltage constraints of the form $v_{\min} \le v_k \le v_{\max}$ can be written as

$$G_1 v_k \le g_1, \quad G_1 = \begin{bmatrix} I \\ -I \end{bmatrix}, \quad g_1 = \begin{bmatrix} v_{\max} \\ -v_{\min} \end{bmatrix} \tag{23}$$

In order to express this as a constraint on the optimization variable $\widehat{U}$ we project the constraint N steps into the future and substitute the linearization $v = v_0 + u$ to obtain

$$\widehat{G}_1 \widehat{U} \le \widehat{g}_1 - \widehat{G}_1 \widehat{v}_0 \tag{24}$$

Here, and throughout the remainder of this section we use the hat notation to indicate the repetition of a vector or the block-diagonal repetition of a matrix, N steps into the future. That is

$$\widehat{G}_1 := \mathrm{blockdiag}(\underbrace{G_1 \dots G_1}) \times N \quad \widehat{g}_1 := \left[\underbrace{g_1^T \dots g_1^T}\right] \times N^T \quad \widehat{v}_0 := \left[\underbrace{v_0^T \dots v_0^T}\right] \times N^T \tag{25}$$

Input rate constraints: We also limit the change in step size that the applied input voltages may take. This is an input rate constraint of the form

$$G_2 \Delta v_k \le g_2 \tag{26}$$

which can be written in terms of the optimization variable $\widehat{U}$ by recognizing that $\widehat{v} = \widehat{v}_0 + \widehat{U}$ and

$$\Delta \widehat{v}_k = \underbrace{\begin{bmatrix} I & & & \\ -I & I & & \\ & \ddots & & \\ & & -I & I \end{bmatrix}}_{S_v} \begin{bmatrix} v_k \\ v_{k+1} \\ \vdots \\ v_{k+N-1} \end{bmatrix} - \underbrace{\begin{bmatrix} v_{k-1} \\ 0 \\ \vdots \\ 0 \end{bmatrix}}_{v_{\mathrm{prev}}} \tag{27}$$

The constraint projected into the future becomes

$$\widehat{G}_2 S_v \widehat{U} \le \widehat{g}_2 - \widehat{G}_2 S_v \widehat{v}_0 + \widehat{G}_2 v_{\mathrm{prev}} \tag{28}$$

Power and power derivative: It was found that the power constraint can be met easily without constraints, but the power derivative constraint must be included explicitly.

The power derivative constraint is not affine since it depends on the product of the state and input $P = I_c^T v$. However, it can be approximated as such by noting that the coil currents evolve much more slowly than the applied voltage inputs giving

$$\dot{P} = \dot{I}_c^T v + I_c^T \dot{v} \approx I_c^T \dot{v} \approx \frac{1}{t_s} I_c^T \Delta v \tag{29}$$

where the sample time t_s of the discrete state-space model is used. This is a special case of input rate constraint Eq. (26), and is implemented with a small margin to account for the nonlinearities that were dropped.

*State and output constraints:*Since the measured outputs (Eq. (9)) include the PF coil currents, state and output constraints are handled identically. We evaluate constraints of the form

$$G_3 e \le g_3 \tag{30}$$

Substituting the prediction model Eq. (21) and the linearization $e = e_0 + y$, the constraint formulation becomes

$$\widehat{G}_3 F \widehat{U} \le \widehat{g}_3 - \widehat{e}_0 - \widehat{G}_3 E x_k \tag{31}$$

The model predictive controller is now fully defined by the cost function Eq. (22) and the constraints Eqs. (24), (28), (31).

4. Measurement and process noise

We also simulate the inclusion of measurement and process noise. The controller handles this noise by means of Kalman filtering. The state equations under consideration are

$$\begin{aligned} x_{k+1} &= \mathrm{A}x_k + \mathrm{B}u_k + w_k \\ y_k &= \mathrm{C}x_k + v_k \end{aligned} \tag{32}$$

The vectors w and v correspond to process noise and measurement noise respectively. The Kalman filter gives a recursive algorithm to define estimator states $\bar{x}$ and estimated outputs $\bar{y} = C\bar{x}$. Then the control algorithm is implemented using only the *estimated* states and outputs. To implement the Kalman filter we first define the noise covariance matrices

$$Q = \mathbb{E}[w_k w_k^T], \quad R = \mathbb{E}[v_k v_k^T], \quad P_{k|k} = \mathbb{E}[(x_k - \bar{x}_k)(x_k - \bar{x}_k)^T] \tag{33}$$

The filter is recursive which leaves the problem of identifying an initialization for the error covariance matrix $P_{k|k}$. We can take $P_{0|0} = \rho Q$ where ρ is a scalar greater than 1, here set to 10. The algorithm can be divided into steps as follows:

First, the error covariance matrix is predicted one step into the future

$$P_{k+1|k} = \mathrm{A}P_{k|k}A^T + Q \tag{34}$$

Second, the optimal Kalman gain is found via

$$\begin{aligned} S_k &= \mathrm{C}P_{k+1|k}C^T + R \\ K_k &= P_{k+1|k}C^T S_k^{-1} \end{aligned} \tag{35}$$

Lastly, we project the system one step into the future. The error covariance matrix and estimator states are updated as

$$\begin{aligned} P_{k+1|k+1} &= (I - K_k C)P_{k+1|k} \\ \bar{x}_{k+1} &= A\bar{x}_k + \mathrm{B}u_k + K_k r_k \end{aligned} \tag{36}$$

The residual term r_k represents the difference between measured and predicted outputs and is normally taken as $r_k = y_k - C\bar{x}_k$. However, the goal is to have state convergence in the unlinearized frame as discussed in [32], so we use the unlinearized outputs to determine the residual. We take

$$r_k = (y_k + e_0) - (C\bar{x}_k + \overline{e_0}) \tag{37}$$

where $\overline{e_0}$ is the estimated error at the most recent linearization. Eq. (36) highlights the effect of the Kalman filter. The estimator states are integrated forward in time according to the state-space model Eq. (32), but with a correction term dependent on the residual. The Kalman gain matrix K_k indicates how much the residual error should affect the state estimate.

Table 2 indicates the standard deviations of measurement and process noise for the simulation parameters. For plasma current, the standard deviation σ is estimated using the specification for the Continuous External Rogowski (CER) coil diagnostic $\sigma = 0.005 \times I_p$ according to Eq. (2) of [33]. The coil current noise levels are estimated according to the same relation. Table 2 of [34] gives noise levels for current centroid position normalized to minor radius z_c/a for various machines. Assuming $z_c/a = 0.01$ and that x-point and strike point positions are measured with a similar accuracy gives the standard deviation levels of 2 cm. The noise levels presented here are a first-order estimate and are not expected to represent the full diagnostic and reconstruction capability for ITER.

5. Simulation results

In this section we perform nonlinear simulations of the controller for high flux expansion scenarios. At every time step, we solve the free-boundary Grad–Shafranov equation using the circuit currents as boundary conditions, and re-linearize the system to determine the $A(t)$, $B(t)$, and $C(t)$ matrices of the isoflux model (Eq. (5)). The MPC algorithm optimizes to obtain a set of coil voltages and the currents are then integrated forward in time.

5.1. Scenario: flux expansion control

In this scenario we consider a plasma that is limited by the shadowing effect of the monoblocks as discussed in the Introduction. In this case we control the flux expansion directly, as opposed to indirectly via the position of a secondary x-point (which does not exist). The flux expansion is defined

$$f_{\mathrm{exp}} = \frac{(\mathrm{RB}_p)_{\mathrm{mp}}}{(\mathrm{RB}_p)_{\mathrm{sp}}} = \frac{|\nabla\psi|_{\mathrm{mp}}}{|\nabla\psi|_{\mathrm{sp}}} \tag{38}$$

Table 2
Measurement and process noise levels standard deviations used for state estimation of the system Eq. (32) with a sample time of 200 ms.

Kalman filter noise (ts = 200 ms)		
	Measurement v_k	Process w_k
I_c	$0.005\,\max(I_c)$	$5 \times 10^{-4}\,\max(I_c)$
I_p	$0.005\,\max(I_p)$	$5 \times 10^{-4}\,\max(I_p)$
I_v	–	$5 \times 10^{-5}\,\max(I_c)$
r_x	$0.01a$	–
z_x	$0.01a$	–
r_{strike}	$0.01a$	–
r_{strike}	$0.01a$	–
ψ_{bry}	$0.01a\langle\lvert\nabla\psi\rvert\rangle_{cp}$	–
ψ_{cp}	$0.01a\langle\lvert\nabla\psi\rvert\rangle_{cp}$	–

a = ITER minor radius, 2 m.

where the subscripts *mp* and *sp* denote the outer midplane and strike point positions respectively. Taking the derivative, we find the response to changes in the coil currents, which is then included the state-space model equations.

$$\frac{\partial f_{\mathrm{exp}}}{\partial I} = \frac{1}{|\nabla\psi|^2_{\mathrm{sp}}}\left[\frac{1}{f_{\mathrm{exp}}}(\nabla\psi\cdot\nabla\partial_I\psi)_{\mathrm{mp}} - f_{\mathrm{exp}}(\nabla\psi\cdot\nabla\partial_I\psi)_{\mathrm{sp}}\right] \tag{39}$$

Fig. 4 shows results for tracking a series of flux expansion step targets in an $I_p = 15$ MA, $\beta_p = 0.6$, $l_i = 0.9$ plasma. Note that for these equilibria, the strike point angle can be approximated $\theta_{\mathrm{sp}} = 6.2 f_{\mathrm{exp}}^{-1}$, so that the maximum $f_{exp} = 6.5$ corresponds to $\theta < 1^\circ$. We observe that for step changes $\delta f_{exp} = 1.85$, the shape is held fairly constant with a maximum isoflux error of 5 Wb corresponding to ≈10 cm at the control points.

To accommodate the step changes, the power supply voltages max out, accelerating then decelerating the coil currents. Allowing these maximum voltages results in settling times of 20 s for each step change. The coil current limits are also a constraining factor for f_{exp} tracking, with coils PF1 and CS3L both reaching their limits (Fig. 4d). This was found to be a common trend for the CS3L coil, where there is competition between satisfying the CS3L limit and having high f_{exp} and high I_p.

5.2. Pathway to the x-divertor

In this scenario we simulate a control pathway for achieving the maximally flux-expanding x-divertor, in which the secondary x-point is placed at the outer strike point. It is shown that it is possible to achieve the pure XD using the existing power supply and coil designs with an $I_p = 10$ MA plasma. (At higher I_p it becomes increasingly difficult if not impossible to realize the pure XD). This is of course an extreme scenario and presumes that a 1° limit on the strike point can be overcome, perhaps by one of the mechanisms discussed in the introduction. Thus Fig. 6 represents a near-upper limit for the f_{exp} and flaring at the divertor, from which any detachment benefits may occur.

In the inductive current scenario, primary x-point formation is planned to occur at $Ip = 4$ MA [35]. We begin control at this point, starting with a standard diverted plasma at 4 MA and create the secondary x-point (see Fig. 1). That is, we define a target location for the secondary x-point between coils PF5 and PF6 and control the flux gradient to zero at this location. After the x-point is created ($t = 25$ s), we give up control of the flux level near the x-point and begin position control. The secondary x-point follows a predefined trajectory upwards to the outer strike point. At the same time, the coils are used to inductively drive the plasma current to 10 MA. See Fig. 3 for the visualization, and Fig. 5for the time traces.

The controller forms the secondary x-point within a few cm of the desired location (Fig. 1) and is then capable of tracking it up to the outer strike point. The maximum tracking error of 17 cm occurs at $t = 40$ s, and occurs simply because other shaping parameters are weighted more heavily or constrained. The position of the primary x-point for example is weighted an order of magnitude higher because its motion can have adverse effects on the heat flux. The primary x-point moves only about 2 cm despite the large changes in divertor flux geometry. The ramp-up target for I_p is also followed closely.

The most limiting constraint is keeping the outer strike point positioned on the outer wall of the divertor and is actively constrained by the MPC controller for most of the transition. The final values for flux expansion and divertor index are plotted in Fig. 6 and represent an upper limit for these quantities. The peak values are very sensitive to the final x-point position, (peak f_{exp} could, in theory, reach infinity) but the average values along the divertor plate ($\langle DI_{SOL}\rangle$=2.5 and $\langle f_{exp}\rangle$=35) are more robust.

6. Conclusion

A feasibility study for control of high flux expansion scenarios

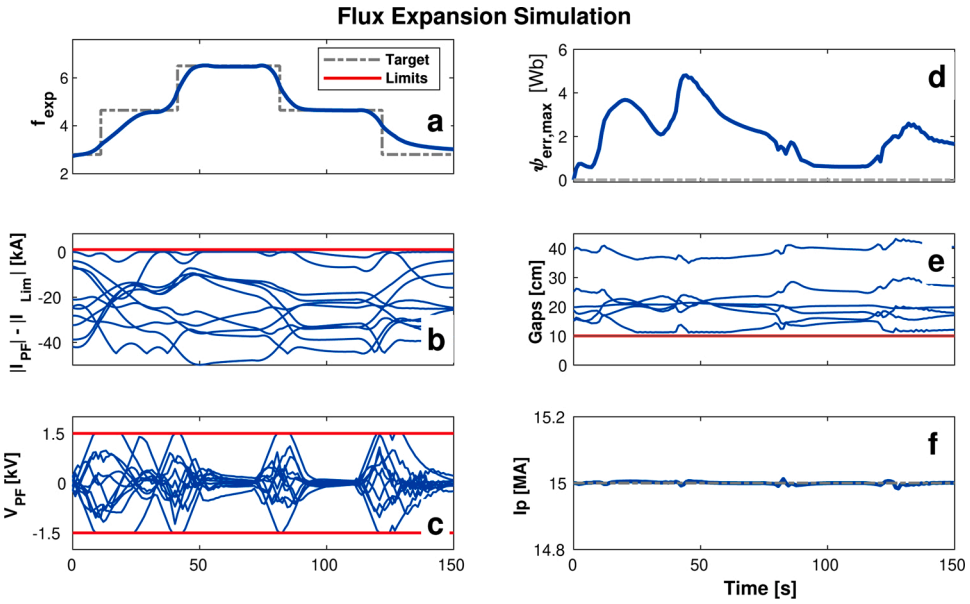

Fig. 4. (a) Tracking step targets for the f_{exp} in a 15 MA plasma. The maximum $f_{exp} = 6.5$ is equivalent to a strike point angle of 0.95°. (b) The proximity of each coil current to its limit, so that a value greater than 0 is a constraint violation. The two coils which reach their limit are PF1 and CS3L. (c) Power supply voltages for each coil. (d) The maximum flux error at the 31 control points. (e) Boundary gaps at a few select locations (inner/outer and lower/midplane/upper). The inner-midplane gap is the most-constricting. (f) Total plasma current.

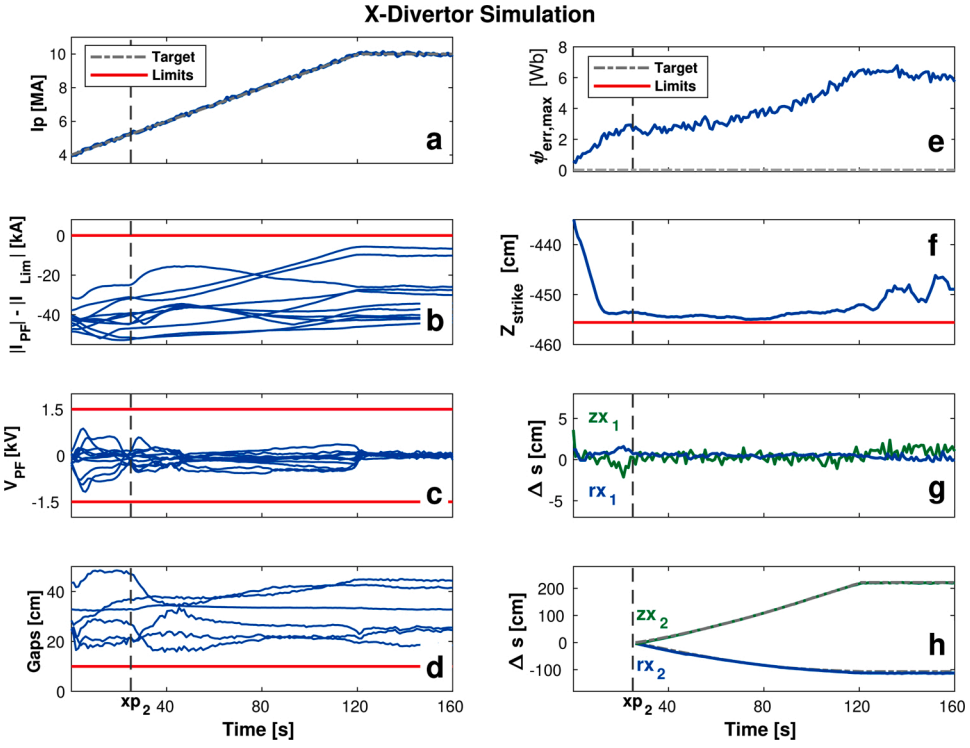

Fig. 5. (a) Rampup trajectory for the plasma current. (b) Proximity of the poloidal field (PF) coil currents to their individual limits, so that values greater than 0 correspond to constraint violations. (c) Power supply voltages applied to the coils. (d) Boundary gaps at a few select locations (inner/outer and lower/midplane/upper). (e) The maximum isoflux error at the 31 control points. (f) The outer strike point position constrains the control for most of the transition. (g) Movement of the primary x-point throughout the transition. (h) Reference-tracking of the secondary x-point throughout the transition.

including an advanced divertor configuration is performed for ITER. This study uses the isoflux shape control model and a model predictive control framework to perform coupled shape and divertor control. We find that the power supplies and coil set are capable of creating and controlling a pure x-divertor (XD) configuration for a 10 MA plasma. One of the limitations of the high flux expansion scenario is that at low strike point angles the plasma wetted area is reduced via shadowing. However, high flux expansion and poloidal flaring, characteristics of the XD, may facilitate enhanced detachment on ITER and negate some of this effect. Thus it would be desirable to operate as close to any flux expansion limit as possible. The controller shows good tracking performance in realizing a reference trajectory for the flux expansion. Results were validated in nonlinear simulation.

Notice

This manuscript is based upon work supported by the U.S. Department of Energy, Office of Science, Office of Fusion Energy Sciences, and has been authored by Princeton University under Contract Number DE-AC02-09CH11466 with the U.S. Department of Energy. The publisher, by accepting the article for publication acknowledges, that the United States Government retains a non-exclusive, paid-up, irrevocable, worldwide license to publish or reproduce the published form of this manuscript, or allow others to do so, for United States Government purposes.

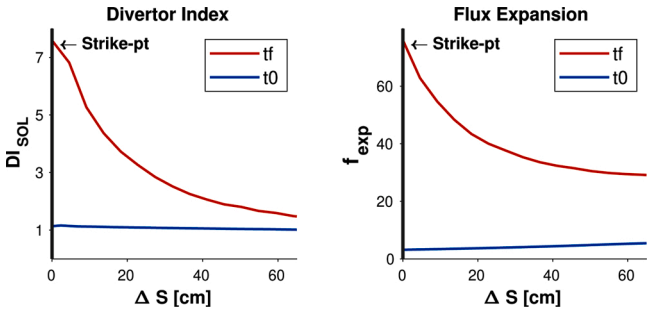

Fig. 6. Measurements along the outer divertor plate of the flaring (DI_{SOL}) and flux expansion at the beginning and end of the simulation. The end-of-simulation results represent a pure XD and a near-upper bound for these parameters.

Authors' contribution

J.T. Wai: methodology, software, validation, writing. P.J. Vail: methodology – creation of models, software – design computer programs. E. Kolemen: methodology, supervision, writing – reviewing and editing, funding.

Conflict of interest

None declared.

Declaration of Competing Interest

The authors report no declarations of interest.

References

[1] P. Scokaert, J. Rawlings, IEEE Trans. Autom. Control 43 (1998) 1163–1169, https://doi.org/10.1109/9.704994.
[2] B. Covele, P. Valanju, M. Kotschenreuther, S. Mahajan, Nucl. Fusion 54 (2014) 072006, https://doi.org/10.1088/0029-5515/54/7/072006.
[3] D.D. Ryutov, Phys. Plasmas 14 (2007) 064502, https://doi.org/10.1063/1.2738399.
[4] M. Kotschenreuther, P. Valanju, B. Covele, S. Mahajan, Phys. Plasmas 20 (2013) 102507, https://doi.org/10.1063/1.4824735.
[5] P.M. Valanju, M. Kotschenreuther, S.M. Mahajan, J. Canik, Phys. Plasmas 16 (2009) 056110, https://doi.org/10.1063/1.3110984.
[6] R.A. Pitts, et al., Phys. Scr. T138 (2009) 014001, https://doi.org/10.1088/0031-8949/2009/t138/014001.
[7] J. Menard, et al., Nucl. Fusion 52 (2012) 083015, https://doi.org/10.1088/0029-5515/52/8/083015.
[8] H. Guo, et al., Nucl. Fusion 59 (2019) 086054, https://doi.org/10.1088/1741-4326/ab26ee.
[9] B. Xiao, et al., Fusion Eng. Des. 146 (2019) 2149–2152, https://doi.org/10.1016/j.fusengdes.2019.03.126.
[10] G. Federici, et al.. EU DEMO Design and R&D Studies 2013 IEEE 25th Symposium on Fusion Engineering (SOFE) (IEEE), 2013, https://doi.org/10.1109/sofe.2013.6635288.
[11] K. Lackner, H. Zohm, Fusion Sci. Technol. 63 (2013) 43–48, https://doi.org/10.13182/fst12-520.
[12] Z.P. Chen, M. Kotschenreuther, S. Mahajan, S. Gerhardt, Nucl. Fusion 58 (2018) 036015, https://doi.org/10.1088/1741-4326/aaa5ca.
[13] F. Hofmann, S. Jardin, Nucl. Fusion 30 (1990) 2013–2022, https://doi.org/10.1088/0029-5515/30/10/003.
[14] E. Kolemen, et al., Nucl. Fusion 58 (2018) 066007, https://doi.org/10.1088/1741-4326/aab0d3.
[15] E. Kolemen, et al., J. Nucl. Mater. 463 (2015) 1186–1190, https://doi.org/10.1016/j.jnucmat.2014.11.099.
[16] E. Kolemen, et al., Nucl. Fusion 50 (2010) 105010, https://doi.org/10.1088/0029-5515/50/10/105010.
[17] E. Kolemen, et al., Nucl. Fusion 51 (2011) 113024, https://doi.org/10.1088/0029-5515/51/11/113024.
[18] P.J. Vail, et al., Plasma Phys. Control. Fusion 61 (2019) 035005, https://doi.org/10.1088/1361-6587/aaf94a.
[19] V.A. Soukhanovskii, Plasma Phys. Control. Fusion 59 (2017) 064005, https://doi.org/10.1088/1361-6587/aa6959.
[20] B. Lipschultz, F.I. Parra, I.H. Hutchinson, Nucl. Fusion 56 (2016) 056007, https://doi.org/10.1088/0029-5515/56/5/056007.
[21] G. Ambrosino, et al.. Plasma Position and Shape Control in ITER Using In-Vessel Coils 2008 47th IEEE Conference on Decision and Control (IEEE), 2008, https://doi.org/10.1109/cdc.2008.4738711.
[22] V. Belyakov, et al., Fusion Eng. Des. 45 (1999) 55–64, https://doi.org/10.1016/s0920-3796(98)00431-1.
[23] Y.V. Mitrishkin, N.M. Kartsev. Hierarchical Plasma Shape, Position, and Current Control System for ITER IEEE Conference on Decision and Control and European Control Conference (IEEE), 2011, https://doi.org/10.1109/cdc.2011.6160443.
[24] S. Gerkšič, G. de Tommasi, Fusion Eng. Des. 88 (2013) 1082–1086, https://doi.org/10.1016/j.fusengdes.2013.02.021.
[25] S. Gerksic, et al.. ITER Plasma Current and Shape Control Using MPC 2016 IEEE Conference on Control Applications (CCA) (IEEE), 2016, https://doi.org/10.1109/cca.2016.7587895.
[26] A. Portone, et al., Fusion Technol. 32 (1997) 374–389, https://doi.org/10.13182/fst97-a2.
[27] R. Albanese, et al., Fusion Technol. 30 (1996) 167–183, https://doi.org/10.13182/fst96-a30749.
[28] A.S. Welander, et al., Fusion Sci. Technol. 47 (2005) 763–767, https://doi.org/10.13182/fst05-a778.
[29] D. Humphreys, et al., Fusion Eng. Des. 83 (2008) 193–197, https://doi.org/10.1016/j.fusengdes.2008.01.012.
[30] R. Keys, IEEE Trans. Acoust. Speech Signal Process. 29 (1981) 1153–1160, https://doi.org/10.1109/tassp.1981.1163711.
[31] S. Gerkšič, et al., Fusion Eng. Des. 129 (2018) 158–163, https://doi.org/10.1016/j.fusengdes.2018.01.074.
[32] M.L. Walker, D.A. Humphreys, Fusion Sci. Technol. 50 (2006) 473–489, https://doi.org/10.13182/fst06-a1271.
[33] A. Quercia, et al., Nucl. Fusion 57 (2017) 126049, https://doi.org/10.1088/1741-4326/aa86fd.
[34] D. Humphreys, et al., Nucl. Fusion 49 (2009) 115003, https://doi.org/10.1088/0029-5515/49/11/115003.
[35] A.C.C. Sips, et al., Phys. Plasmas 22 (2015) 021804, https://doi.org/10.1063/1.4904015.